IEEE Access
Multidisciplinary ⋮ Rapid Review ⋮ Open Access Journal

Received August 3, 2018, accepted September 11, 2018, date of publication September 17, 2018, date of current version October 12, 2018.

Digital Object Identifier 10.1109/ACCESS.2018.2870411

A Robust Control Strategy Research on PMSG-Based WECS Considering the Uncertainties

FEIHANG ZHOU AND JUN LIU
College of Automation, Xi'an University of Technology, Xi'an, China
Corresponding authors: Feihang Zhou (qq987102679@126.com) and Jun Liu (liujun0310@sina.com)

This work was supported in part by the Key R & D Project, Shaanxi, China, under Grant 2017GY-061.

ABSTRACT This paper proposes a robust control strategy for the uncertainties of permanent magnet synchronous generator-based wind energy conversion system, based on state feedback. Meanwhile, the detailed design and analysis process of this robust controller also have been presented. Compared with the conventional control, the new method with a better robustness can not only make the whole closed-loop system stable but also reduce the major harmonics and total harmonic distortion of currents and ripples of torque. And then, we set up a detailed 2 MW simulation test platform based on MATLAB/SIMULINK/SimPowerSysterms. The simulation results verify the effectiveness and correctness of the algorithm.

INDEX TERMS Robust control strategy, state feedback, PMSG, WECS, robustness, THD.

I. INTRODUCTION

With the global climate problem increasingly prominent and non-renewable energy sources being largely consumed, the exploration and utilization of renewable energy sources have been paid to a high attention. As the fastest growing renewable energy sources in the recent years [1], wind generation is most prevalent in coastal regions spanning temperate and boreal climates. Countries such as China, USA, Denmark and Canada possess significant wind power potential due to their high average wind velocities [2]. Hence, the research and development about wind power have much practical value nowadays. Compared with the constant-speed constant-frequency WECS, the greatest advantages of variable-speed constant-frequency WECS is able to get access to the maximum energy conversion. Mainstream generator models of variable-speed constant-frequency WECS include doubly-fed induction generator (DFIG) and permanent magnet synchronous generator (PMSG). Compared with DFIG, PMSG has many superior characteristics such as more efficient performance, higher reliability and wider speed control range, and is gradually becoming the first choice [3]. Therefore, we selected the WECS based on PMSG for a research in this paper.

There exist many uncertainties in practical systems. For the PMSG or permanent-magnet synchronous motor (PMSM), the uncertainties consist of the parameter perturbations, the unmodeled converter dynamics and the load torque enter system via different channels from the control inputs [4]–[7]. Reference [4] introduced a robust control scheme for the uncertainties of PMSM with a adaptive disturbance observer and the controller obtained a good control performance. Reference [5] once proposed a robust nonlinear predictive controller for the PMSM uncertainties. The high performance with respect to speed tracking and current control has been demonstrated. Reference [6] studied the predictive functional control (PFC) and extended state observer (ESO) for the uncertainties of PMSM and verified the effectiveness of PFC + ESO method. For the PMSG-based WECS, Reference [7] presented a novel decoupled PI current control method. The technique can successfully achieve the nominal performance recovery under the model uncertainty as well as improved the transient performances. References [8]–[12] applied sliding mode control (SMC) to WECS and achieved a good control effect. Reference [8] proposed a direct power control (DPC) based on SMC for the grid-connected WECS with driven doubly fed induction generators (DFIG). The controller is able to directly regulate the instantaneous reactive and active powers in stator stationary reference frame without the requirement of either synchronous coordinate transformation or phase angle tracking of grid voltage and can still achieve a good control performance, when the grid voltage is unbalanced. For the WECS based on PMSG,

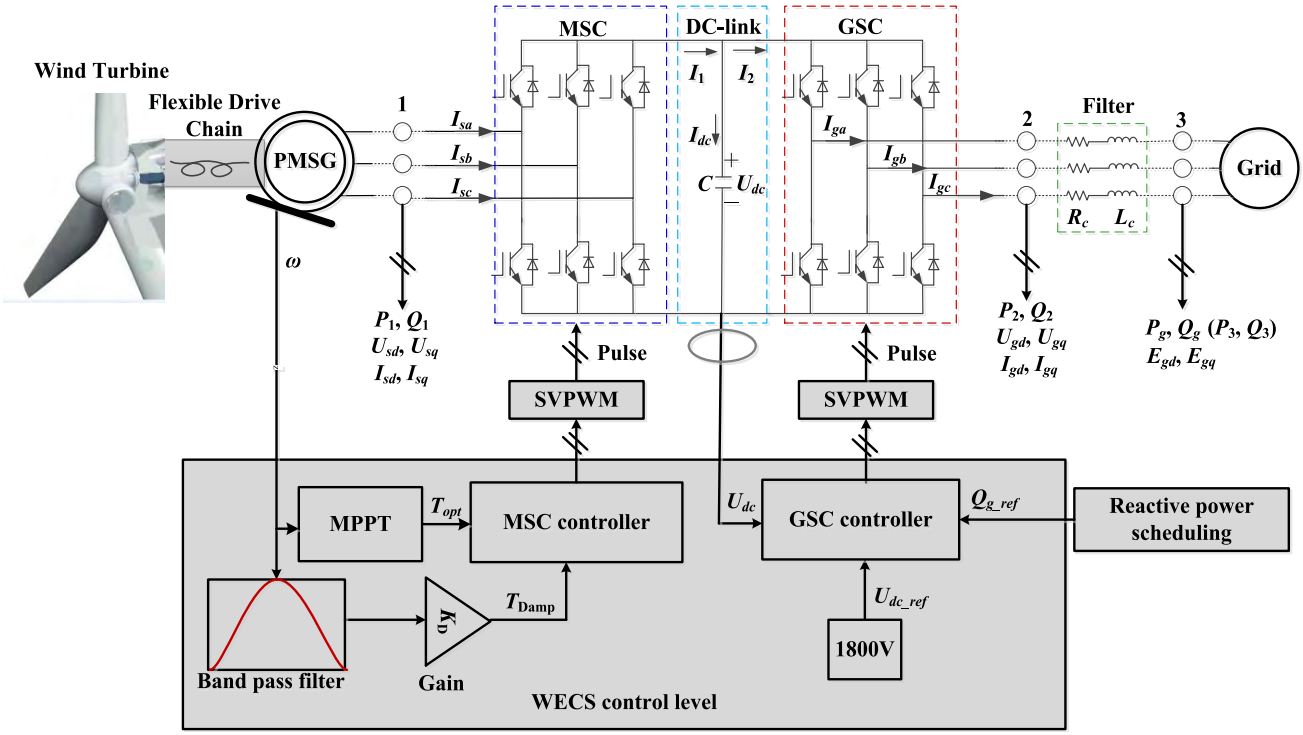

FIGURE 1. Configuration of a WECS.

reference [9] improved the control performance and efficiency of SMC by enhancing the exponential reaching law. Reference [10] explored an adaptive second-order SMC strategy to maximize the energy production of WECS simultaneously reducing the mechanical stress on the drive chain. This method can successfully deals with the random wind, intrinsic nonlinear behavior of WECS, and the presence of model uncertainties and external perturbations acting on the system. Reference [11] developed a SMC approach for systems with mismatched uncertainties via a nonlinear disturbance observer (DOB). the strategy also exhibited a good control performance. The integral sliding-model control (I-SMC) is mentioned in [12]. Compared with the SMC, the I-SMC can get a better steady-state precision and more practical application. With the introduction of these new methods, the research on WECS control strategies will be more in-depth. Therefore, this paper also aims at studying the new control strategy for WECS.

In general, wind power system control technology consists of outer control and inner control. This paper mainly considers the inner loop current control of WECS. The structure of this paper as follow:

- Firstly, the structure and models of WECS is briefly introduced and the state space model considering system uncertainties is established.
- Then, the control objectives are also be given. In this part, the suppression of flexible drive chain torsional vibration is considered. And the conventional method of torsional vibration suppression [13]–[21] is used here.
- After that, a robust controller for the uncertainties has been proposed based on the state space model. The detailed design and analysis process were described.
- Finally, a detailed simulation test platform based on MATLAB/SIMULINK/SimPowerSysterms is established to verify the effectiveness of the proposed scheme.

Simulation results implies that the robust control strategy can also reduce the and major harmonics and THD of currents and decrease the ripples of torque effectively. This illustrates that the proposed control strategy has a good robustness for the system uncertainties.

II. WIND POWER MATHEMATICAL MODEL

The simplified WECS based on PMSG is mainly consist of a wind turbine, a flexible drive chain, a PMSG, a two back-to-back voltage source converters (VSCs), and the control level by FIGURE 1. In the loop control level, the control of machine side converter (MSC) is to capture the maximum wind energy and the control of grid side converter (GSC) is to keep DC-link voltage U_{dc} stable at 1800V and regulate the reactive power. The maximum power point tracking (MPPT) strategy of optimal torque control (OTC) widely used in the practical engineering application is

adopted here. Meanwhile, the damping compensation torque T_{Damp} is introduced to suppress the torsional vibration of flexible drive chain.

A. DYNAMIC MODEL OF PMSG AND MSC

Considering the uncertainties of the system, the mathematical model of PMSG [22], [23] is

$$\begin{cases} L_{sd}\dfrac{\mathrm{d}I_{sd}}{\mathrm{d}t} = -R_s I_{sd} + n_p\omega L_{sq} I_{sq} + U_{sd} - \varepsilon_{sd} \\ L_{sq}\dfrac{\mathrm{d}I_{sq}}{\mathrm{d}t} = -R_s I_{sq} - n_p\omega L_{sd} I_{sd} - n_p\omega\psi + U_{sq} - \varepsilon_{sq} \end{cases} \tag{1}$$

where I_{sd} and I_{sq} are the d-axis and q-axis stator currents respectively. U_{sd} and U_{sq} are the stator d-axis and q-axis components of the armature voltage. ψ represents the permanent magnet chain. And the disturbance ε_{sd} and ε_{sq} represent model uncertainty, such PWM offset, and external disturbances, and they are assumed to be bounded

$$|\varepsilon_{sd}| \le D_{sd}; \quad |\varepsilon_{sd}| \le D_{sq} \tag{2}$$

The electromagnetic torque is given by

$$T_g = 1.5 n_p \left[(L_{sd} - L_{sq}) I_{sd} I_{sq} + \psi I_{sq}\right] \tag{3}$$

D_{sd} and D_{sq} are the boundaries of ε_{sd} and ε_{sq}.

B. DYNAMIC MODEL OF GSC

Considering the uncertainties of the system, the dynamic model of grid side inverter is given by

$$\begin{cases} L_c\dfrac{\mathrm{d}I_{gd}}{\mathrm{d}t} = -R_c I_{gd} + \omega_g L_c I_{gq} - E_{gd} + U_{gd} - \varepsilon_{gd} \\ L_c\dfrac{\mathrm{d}I_{gq}}{\mathrm{d}t} = -R_c I_{gq} - \omega_g L_c I_{gd} - E_{gq} + U_{gq} - \varepsilon_{gq} \end{cases} \tag{4}$$

where I_{gd} and I_{gq} are the d-axis and q-axis grid side currents respectively. U_{gd} and U_{gq} are control voltage. ω_g is the frequency of power grid. E_{gd} and E_{gq} express the d-axis and q-axis components of power grid potential. If the power grid potential is defined to the d-axis, hence $E_{\mathrm{gq}} = 0$. The ω_g and E_{gd} can be gotten by a voltage phase-locked loop. ε_{gd} and ε_{gq} are also the uncertainty, and meet

$$\left|\varepsilon_{gd}\right| \le D_{gd}; \quad \left|\varepsilon_{gd}\right| \le D_{gq} \tag{5}$$

D_{gd} and D_{gq} are the boundaries of ε_{gd} and ε_{gq}. The active power and reactive power of grid can be expressed as

$$\begin{cases} P_g = E_{gd} I_{gd} + E_{gq} I_{gq} = E_{gd} I_{gd} \\ Q_g = E_{gd} I_{gq} - E_{gq} I_{gd} = E_{gd} I_{gq} \end{cases} \tag{6}$$

C. STATE SPACE MODEL

According to (1) and (4), we can get

$$\boldsymbol{M}\dot{\boldsymbol{x}} + \boldsymbol{C}_1\boldsymbol{x} + \boldsymbol{C}_2\boldsymbol{x} + \boldsymbol{N} = \boldsymbol{u} - \boldsymbol{\varepsilon} \tag{7}$$

where

$$\boldsymbol{x} = \left[\, I_{sd} \;\; I_{sq} \;\; I_{gd} \;\; I_{gq} \,\right]^{\mathrm{T}} \tag{8}$$

$$\boldsymbol{u} = \left[\, U_{sd} \;\; U_{sq} \;\; U_{gd} \;\; U_{gq} \,\right]^{\mathrm{T}} \tag{9}$$

and

$$\boldsymbol{\varepsilon} = \left[\, \varepsilon_{sd} \;\; \varepsilon_{sq} \;\; \varepsilon_{gd} \;\; \varepsilon_{gq} \,\right]^{\mathrm{T}} \tag{10}$$

The matrix $\boldsymbol{M}$, $\boldsymbol{C}_1$ and $\boldsymbol{C}_2$ are the 4×4 constant matrixs, and they are given by

$$\boldsymbol{M} = \boldsymbol{M}^{\mathrm{T}} = diag\left(L_{sd}, L_{sq}, L_c, L_c\right) \tag{11}$$

$$\boldsymbol{C}_1 = \boldsymbol{C}_1^{\mathrm{T}} = diag\left(R_s, R_s, R_c, R_c\right) \tag{12}$$

$$\boldsymbol{C}_2 = \begin{bmatrix} 0 & -n_p\omega L_{sq} & 0 & 0 \\ n_p\omega L_{sd} & 0 & 0 & 0 \\ 0 & 0 & 0 & -\omega_g L_c \\ 0 & 0 & \omega_g L_c & 0 \end{bmatrix} \tag{13}$$

where L_{sd} and L_{sq} are the d-axis and q-axis stator inductances. R_{s} is the stator resistance. n_{p} represents magnetic pole logarithms. ω is the rotor speed. For the non-salient PMSG, the stator inductances meet $L_{sd} = L_{sq} = L$. Therefore,

$$\boldsymbol{C}_2 = -\boldsymbol{C}_2^{\mathrm{T}} \tag{14}$$

The vector $\boldsymbol{N}$ is defined as follows

$$\boldsymbol{N} = \left[\, 0 \;\; n_p\omega\psi \;\; E_{gd} \;\; E_{gq} \,\right]^{\mathrm{T}} \tag{15}$$

III. CONTROLLER DESIGN

A. CONTROL OBJECTIVES

The main control objective of WECS is maximum power point tracking (MPPT), when the wind speed below rated wind speed. The optimal torque control (OTC) [24], [25] as one of the MPPT methods, is widely used in the practical engineering application. The optimal torque T_{opt} is chosen as

$$\begin{cases} T_{opt} = K_{opt}\omega^2 \\ K_{\mathrm{opt}} = 0.5\pi\rho R^5 C_{P\_\max} \Big/ \lambda_{opt}^3 \end{cases} \tag{16}$$

where ρ is the air density. R is the radius of wind wheel. C_{P_max} is defined as the maximum wind energy conversion coefficient. λ_{opt} is the optimal tip speed ratio (OTSR).

For the flexible drive chain, the electrical damping needs to be injected to suppress torsional vibration. In general, the process of injecting damping can be divided into two steps. Firstly, we should extract torsional vibration information from generator speed signal by a bandpass filter. And then, the extracted torsional vibration information is multiplied by a magnification K_D and introduced the torque control loop. The gain K_D is the value of the actual injection damping. The amplitude frequency curve of bandpass filter is shown in FIGURE 2.

Usually, the transfer function of bandpass filter is

$$H(s) = \frac{2\zeta s/\Omega_0}{s^2/\Omega_0^2 + 2\zeta s/\Omega_0 + 1} \tag{17}$$

where s is the Laplace variable. ζ is the damping ratio.

If $s = j\Omega$, we can get

$$\begin{aligned} G(j\Omega) &= |G(j\Omega)| \angle\theta \\ &= \frac{2\zeta\Omega/\Omega_0}{\sqrt{(1-\Omega^2/\Omega_0^2)^2 + (2\zeta\Omega/\Omega_0)^2}} \\ &\quad \angle\left(90^{\mathrm{o}} - \arctan\frac{2\zeta\Omega/\Omega_0}{1-\Omega^2/\Omega_0^2}\right) \end{aligned} \tag{18}$$

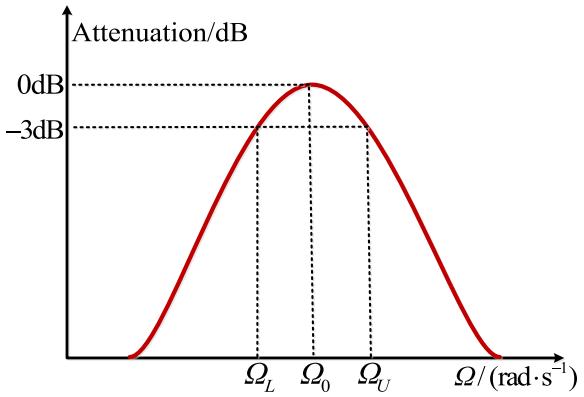

FIGURE 2. Amplitude frequency curve of bandpass filter. Remark: Ω_0 is the center frequency, Ω_U is the upper cut-off frequency and Ω_L is the low center frequency.

and

$$\lim_{\Omega\to 0}|G(j\Omega)|=0 \quad \text{and} \quad \lim_{\Omega\to\infty}|G(j\Omega)|=0 \tag{19}$$

Usually, the bandwith BW of the bandpass filter is given by

$$BW=\frac{\zeta\Omega_0}{\pi} \tag{20}$$

Hence, the damping compensation torque is

$$T_{Damp}=K_D H(s)\,\omega \tag{21}$$

where K_D is the injected damping.

The back to back dual PWM full power converter is used in the WECS. And the reference currents of MSC can be written as

$$\begin{cases} I_{sd\_ref}=0 \\ I_{sq\_ref}=\dfrac{2}{3}\times\dfrac{T_{opt}+T_{Damp}}{n_p\psi} \end{cases} \tag{22}$$

where I_{sd_ref} and I_{sq_ref} are the reference signals of d-axis and q-axis stator currents.

The objectives of GSC are to keep the bus voltage at the given value U_{dc_ref} stably and realize a proper reactive power regulation. Here, the reference currents of GSC is given by

$$\begin{cases} I_{gd\_ref}=\left(K_P+\dfrac{K_I}{s}\right)\left(U_{dc\_ref}-U_{dc}\right) \\ I_{gq\_ref}=\dfrac{Q_{g\_ref}}{E_{gd}} \end{cases} \tag{23}$$

where I_{gd_ref} and I_{gq_ref} are the reference signals of d-axis and q-axis grid side currents. K_P and K_I are the proportional-integral (PI) parameters. Q_{g_ref} is the reference of reactive power.

B. ROBUST CONTROLLER DESIGN

According to (7), the error equation is assumed as

$$\boldsymbol{M}\dot{\boldsymbol{e}}+\boldsymbol{C}_1\boldsymbol{e}+\boldsymbol{C}_2\boldsymbol{e}=\boldsymbol{\zeta}+\boldsymbol{\varepsilon} \tag{24}$$

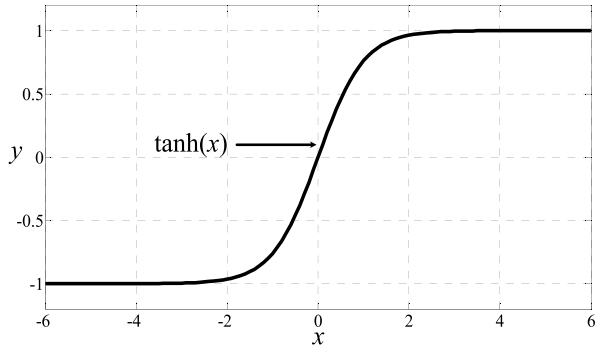

FIGURE 3. The function curve of tanh(x).

where ζ can be considered as a virtual control item and the error vector $\boldsymbol{e}$ is defined as

$$\boldsymbol{e}=\begin{bmatrix} e_{sd} & e_{sq} & e_{gd} & e_{gq}\end{bmatrix}^{\mathrm{T}}=\boldsymbol{x}_{ref}-\boldsymbol{x} \tag{25}$$

The reference vector $\boldsymbol{x}_{ref}$ is

$$\boldsymbol{x}_{ref}=\begin{bmatrix} I_{sd\_ref} & I_{sq\_ref} & I_{gd\_ref} & I_{gd\_ref}\end{bmatrix}^{\mathrm{T}} \tag{26}$$

If the Lyapunov function is defined as

$$V(\boldsymbol{e})=\frac{1}{2}\boldsymbol{e}^{\mathrm{T}}\boldsymbol{M}\boldsymbol{e} \tag{27}$$

then, the derivative of the upper formula is

$$\begin{aligned}\dot{V}(\boldsymbol{e})&=\frac{1}{2}\boldsymbol{e}^{\mathrm{T}}\boldsymbol{M}\dot{\boldsymbol{e}}+\frac{1}{2}(\boldsymbol{M}^{\mathrm{T}}\dot{\boldsymbol{e}})^{\mathrm{T}}\boldsymbol{e}\\ &=\frac{1}{2}\boldsymbol{e}^{\mathrm{T}}(\boldsymbol{\zeta}+\boldsymbol{\varepsilon}-\boldsymbol{C}_1\boldsymbol{e}-\boldsymbol{C}_2\boldsymbol{e})+\frac{1}{2}(\boldsymbol{\zeta}+\boldsymbol{\varepsilon}-\boldsymbol{C}_1\boldsymbol{e}-\boldsymbol{C}_2\boldsymbol{e})^{\mathrm{T}}\boldsymbol{e}\\ &=-\boldsymbol{e}^{\mathrm{T}}\boldsymbol{C}_1\boldsymbol{e}+\frac{1}{2}\left\{\boldsymbol{e}^{\mathrm{T}}(\boldsymbol{\zeta}+\boldsymbol{\varepsilon})+(\boldsymbol{\zeta}+\boldsymbol{\varepsilon})^{\mathrm{T}}\boldsymbol{e}\right\}\\ &=-\boldsymbol{e}^{\mathrm{T}}\boldsymbol{C}_1\boldsymbol{e}+\boldsymbol{e}^{\mathrm{T}}\boldsymbol{\zeta}+\boldsymbol{e}^{\mathrm{T}}\boldsymbol{\varepsilon}\end{aligned} \tag{28}$$

Usually, (29) is established.

$$\begin{cases} e_{sd}\varepsilon_{sd}\le|e_{sd}\varepsilon_{sd}|\le D_{sd}|e_{sd}|=D_{sd}e_{sd}\mathrm{sgn}(e_{sd}) \\ e_{sq}\varepsilon_{sq}\le|e_{sq}\varepsilon_{sq}|\le D_{sq}|e_{sq}|=D_{sq}e_{sq}\mathrm{sgn}(e_{sq}) \\ e_{gd}\varepsilon_{gd}\le|e_{gd}\varepsilon_{gd}|\le D_{gd}|e_{gd}|=D_{gd}e_{gd}\mathrm{sgn}(e_{gd}) \\ e_{gq}\varepsilon_{gq}\le|e_{gq}\varepsilon_{gq}|\le D_{gq}|e_{gq}|=D_{gq}e_{gq}\mathrm{sgn}(e_{gq}) \end{cases} \tag{29}$$

namely

$$\boldsymbol{e}^{\mathrm{T}}\boldsymbol{\varepsilon}=e_{sd}\varepsilon_{sd}+e_{sq}\varepsilon_{sq}+e_{gd}\varepsilon_{gd}+e_{gq}\varepsilon_{gq}\le\boldsymbol{e}^{\mathrm{T}}\boldsymbol{D}\mathrm{sgn}(\boldsymbol{e}) \tag{30}$$

where

$$\boldsymbol{D}=diag\left(D_{sd},D_{sq},D_{gd},D_{gq}\right) \tag{31}$$

$$\mathrm{sgn}(\boldsymbol{e})=\begin{bmatrix}\mathrm{sgn}(e_{sd}) & \mathrm{sgn}(e_{sq}) & \mathrm{sgn}(e_{gd}) & \mathrm{sgn}(e_{gq})\end{bmatrix}^{\mathrm{T}} \tag{32}$$

sgn(·) is the symbolic function.

By the assumption

$$\boldsymbol{\zeta}=-\boldsymbol{K}\boldsymbol{e}-\boldsymbol{D}\mathrm{sgn}(\boldsymbol{e}) \tag{33}$$

we can get

$$\dot{V}(\boldsymbol{e})\le-\boldsymbol{e}^{\mathrm{T}}(\boldsymbol{C}_1+\boldsymbol{K})\boldsymbol{e} \tag{34}$$

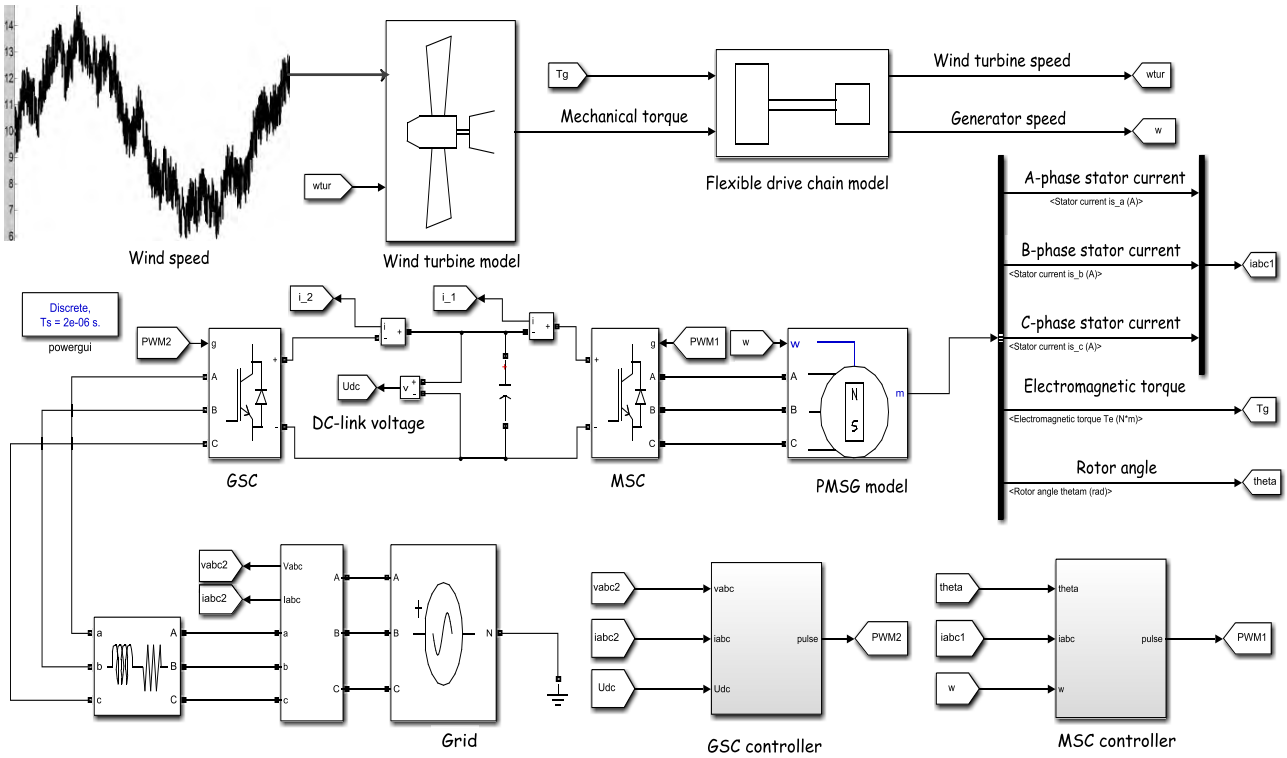

FIGURE 4. Simulation test platform.

If the following formula is established

$$\boldsymbol{C}_1 + \boldsymbol{K} > 0 \tag{35}$$

then,

$$\dot{V}(\boldsymbol{e}) \leq 0 \tag{36}$$

where $\boldsymbol{K}$ is the 4×4 constant matrix.

For the sake of convenience, we set

$$\boldsymbol{C}_1 + \boldsymbol{K} = k\boldsymbol{M} \tag{37}$$

where $k \in R^+$.

Therefore, the control rate $\boldsymbol{u}$ can be gotten by (7), (24) and (33).

$$\boldsymbol{u} = \boldsymbol{M}\dot{\boldsymbol{x}}_{ref} + (\boldsymbol{C}_1 + \boldsymbol{C}_2 + \boldsymbol{K})\boldsymbol{x}_{ref} + \boldsymbol{N} - \boldsymbol{K}\boldsymbol{x} + \boldsymbol{D}\,\mathrm{sgn}(\boldsymbol{e}) \tag{38}$$

Considering the symbolic function can cause the controller chatter, we use the hyperbolic tangent function tanh(·) instead of symbolic function here, due to tanh(·) with the first order continuous derivative. The tanh(x) is

$$\tanh(x) = \frac{e^x - e^{-x}}{e^x + e^{-x}} \tag{39}$$

and the derivative of tanh(x) is

$$\tanh^{(1)}(x) = \frac{4}{\left(e^x + e^{-x}\right)^2} \tag{40}$$

Meanwhile, the function curve of tanh(x) is shown in FIGURE 3. At this time, the control rate $\boldsymbol{u}$ can be rewritten as

$$\boldsymbol{u} = \boldsymbol{M}\dot{\boldsymbol{x}}_{ref} + (\boldsymbol{C}_1 + \boldsymbol{C}_2 + \boldsymbol{K})\boldsymbol{x}_{ref} + \boldsymbol{N} - \boldsymbol{K}\boldsymbol{x} + \boldsymbol{D}\tanh(\boldsymbol{e}) \tag{41}$$

C. PERFORMANCE ANALYSIS OF ROBUST CONTROLLER

According to (27), (34) and (37), (42) can be gotten.

$$\dot{V} \leq -k\boldsymbol{e}^{\mathrm{T}}\boldsymbol{M}\boldsymbol{e} = -2kV \tag{42}$$

Definite integration of (42) between zero and t_{reach} leads to

$$\int_{V(t=0)}^{V(t=t_{\mathrm{reach}})} \frac{\mathrm{d}V}{V} \leq \int_0^{t_{\mathrm{reach}}} -2k\,\mathrm{d}t \tag{43}$$

we can get

$$0 \leq V(t = t_{reach}) \leq V(t = 0)\, e^{-2kt_{reach}} \tag{44}$$

Therefore,

$$\lim_{t_{reach} \to +\infty} V = 0 \tag{45}$$

Due to

$$\boldsymbol{M} = \boldsymbol{M}^{\mathrm{T}} > 0 \tag{46}$$

(47) can be gotten by (27), (45) and (46).

$$\lim_{t \to +\infty} \boldsymbol{e} = \begin{bmatrix} 0 & 0 & 0 & 0 \end{bmatrix}^{\mathrm{T}} \tag{47}$$

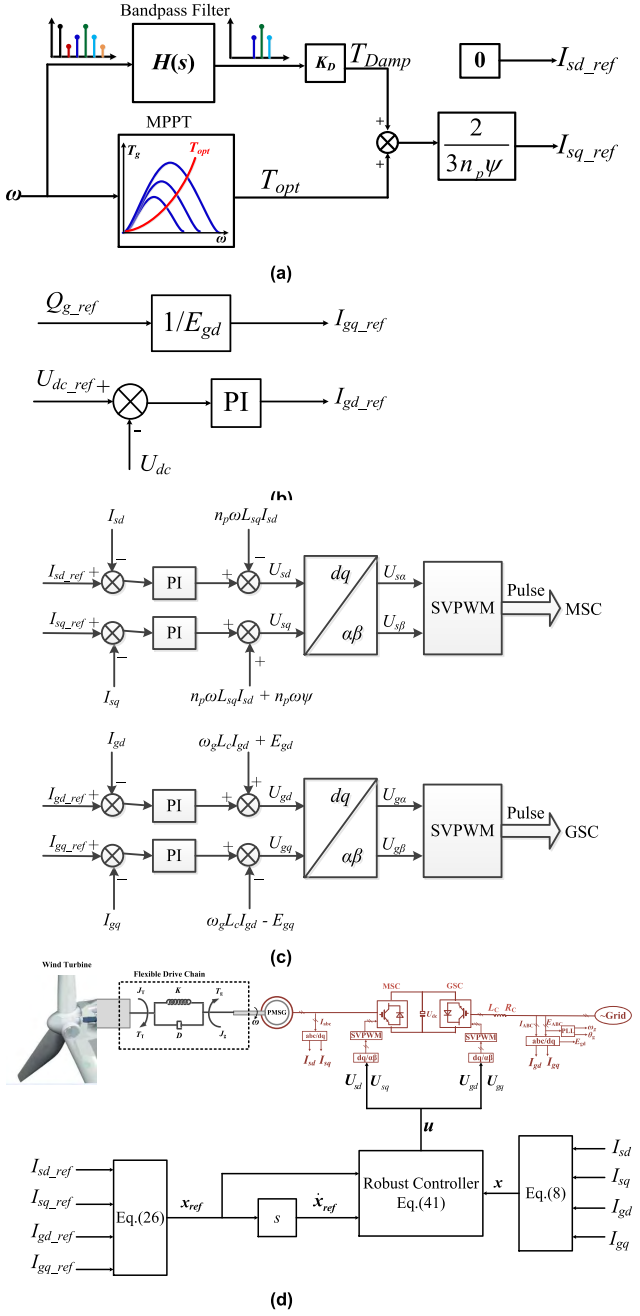

FIGURE 5. Control block diagram of WECS. (a) Torque control. (b) DC-link voltage and reactive power control. (c) Conventional control of inner current loop. (d) Robust control of inner current loop.

This means that steady-state errors of system are zero. In general, if we define

$$\frac{V\left(t=t_{\text{reach}}\right)}{V\left(t=0\right)}=1\% \tag{48}$$

we can get

$$t_{\text{reach}} \leq \frac{1}{2k}\ln\frac{V\left(t=0\right)}{V\left(t=t_{\text{reach}}\right)}=\frac{\ln 10}{k} \tag{49}$$

Obviously, the parameter k determine the response speed of system and the bigger k is, the quicker response speed is.

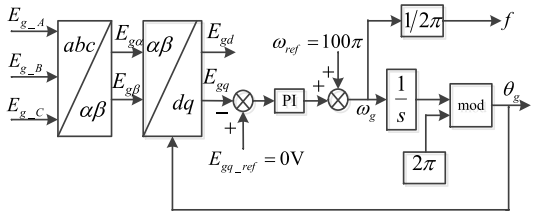

FIGURE 6. Structure diagram of PLL.

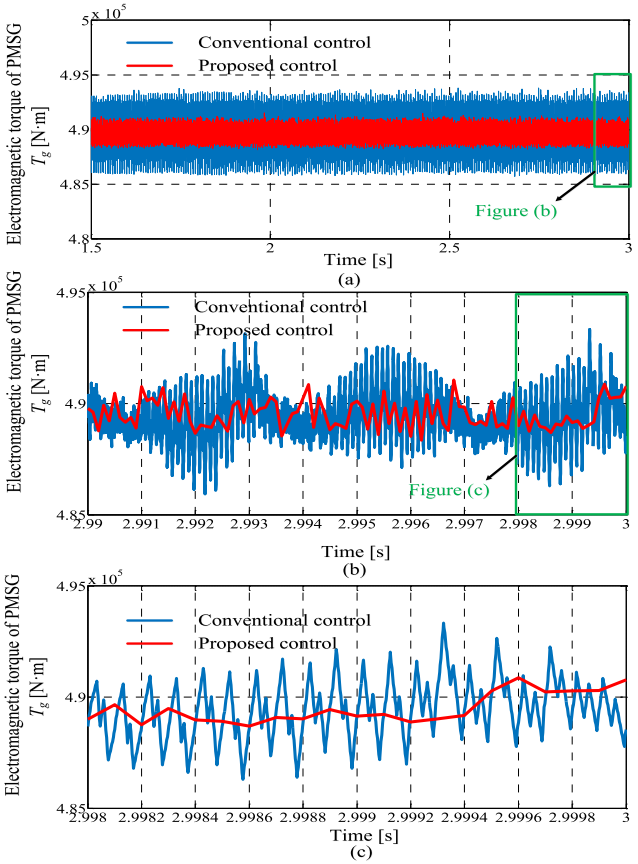

FIGURE 7. PMSG torque curve.

IV. SIMULATION RESULTS

In this section, simulations are carried out based on MATLAB/SIMULINK environment using 2MW PMSG-based WECS, which is connected to infinite-bus electric power system. The packaged modules in SimPowerSysterms were adopted here, including the wind turbine, PMSG, power converters and so on. And, the two mass spring damping model [13]–[21], [23] was used to describe the flexible drive chain. The simulation test platform of the 2MW PMSG-based WECS is shown in FIGURE 4. And the transient response of the system can be obtained under this simulation test platform. The system parameters are shown in Appendix.

FIGURE 5 shows the control block diagram of WECS. The outer loop control is mainly divided into torque control, DC-link voltage control and reactive power control shown

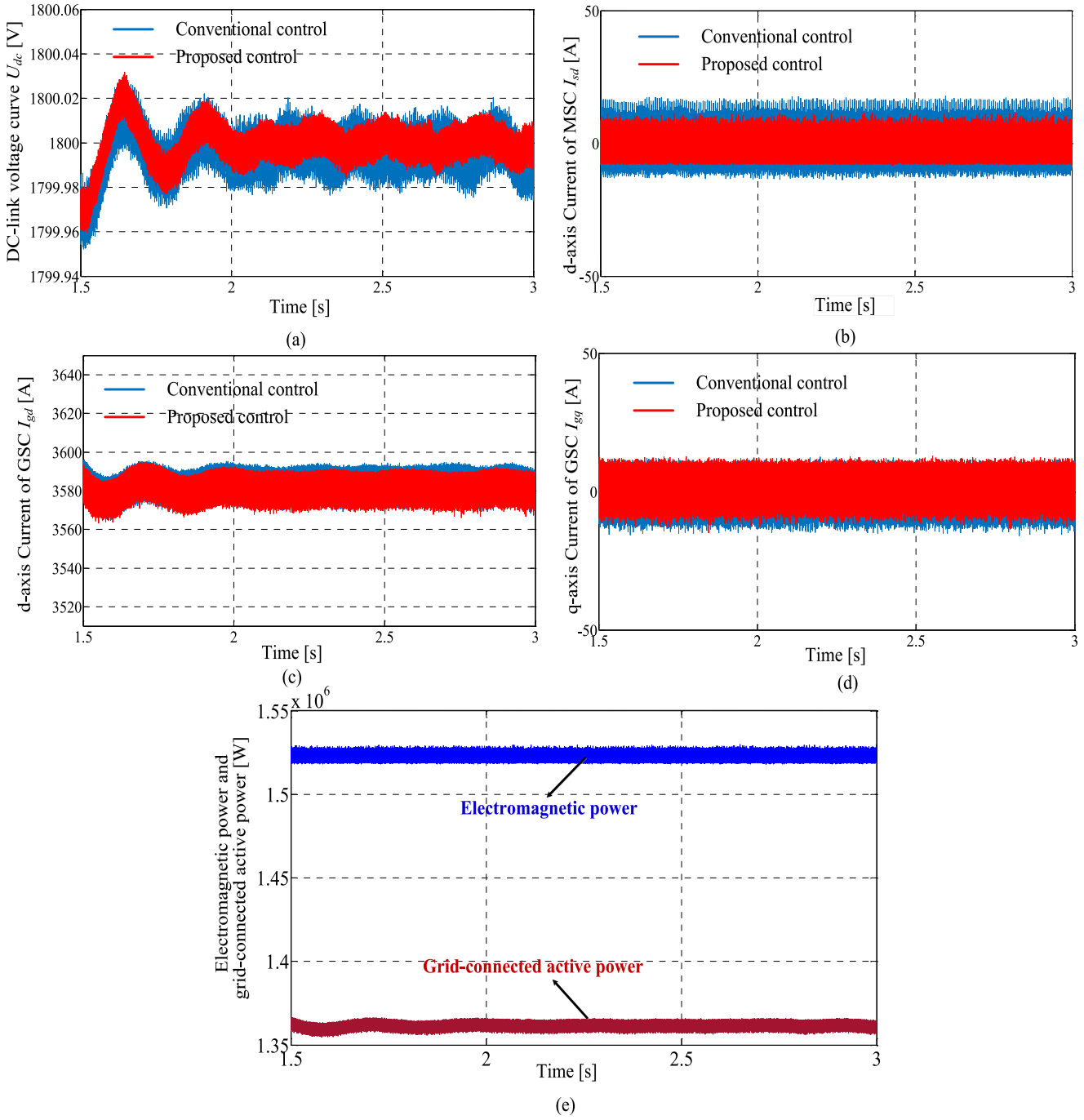

FIGURE 8. System response under constant wind speed.

in FIGURE 5(a) and (b). The damping control of flexible drive and vector control with '$i_d = 0$' were taken into account in torque control. For inner current loop, the strategies of conventional control and proposed control are shown in FIGURE 5(c) and (d). Meanwhile, the structure diagram of voltage phase locked loop (PLL) is shown in FIGURE 6.

A. SIMULATIONS UNDER CONSTANT WIND SPEED

Simulation results under constant wind speed are illustrated in FIGURE 7-9. FIGURE 7 shows the electromagnetic torque curves of PMSG. The introduction of FIGURE 7(b) and FIGURE 7(c) is to observe the electromagnetic transient response in detail. It is clear that the PMSG torque ripple is lower under proposed control, compared with conventional control. From FIGURE 8(a)-(d), we can conclude that the proposed control could reduce the ripples of DC-link voltage, dq-axis MSC currents and dq-axis GSC currents. FIGURE 8(e) shows the curves of electromagnetic power and grid-connected active power. The difference between electromagnetic power and grid-connected active power reflects the

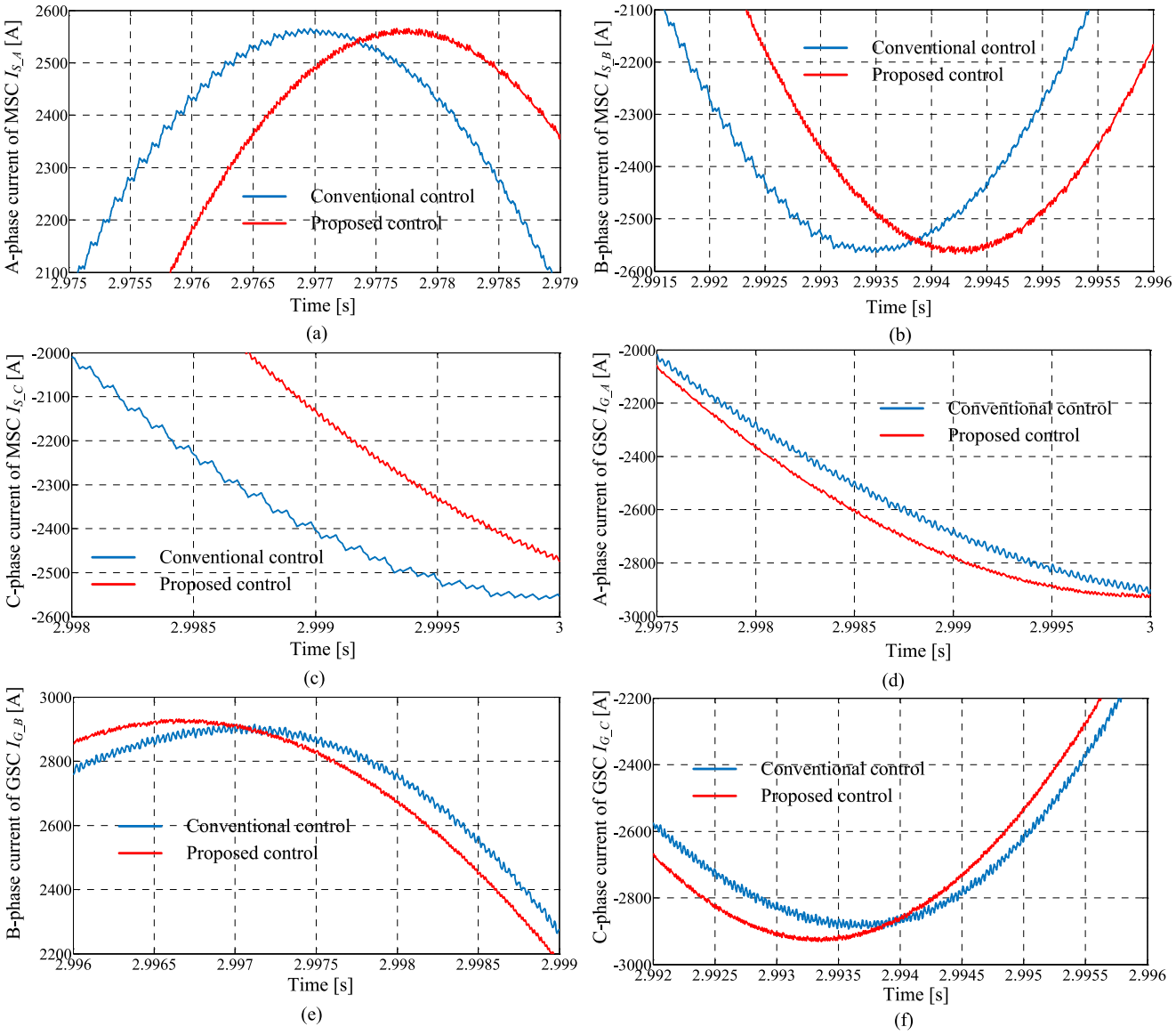

FIGURE 9. Three-phase currents.

copper loss P_{loss_Cu}.

$$P_{loss\_Cu} = R_s\left(I_{sd}^2 + I_{sq}^2\right) + R_c\left(I_{gd}^2 + I_{gq}^2\right)$$

From FIGURE 8(e), the copper loss P_{loss_Cu} is about 160kW. The three-phase currents of MSC and GSC are shown in FIGURE 9. The ripples of three-phase currents are also reduced under proposed control. Furthermore, in order to analyze the currents harmonics, the FFT analysis of three-phase currents were carried out based on Simulink/Powergui. Due to the steady state speed of PMSG is 3.1102 rad/s, then the fundamental frequency should be taken as $n_p\omega/(2\pi) = 50.49$ HZ. After setting the parameters shown in Fig.10, FFT analysis on three-phase currents can be performed. FIGURE 11 and 12 show the FFT analysis of MSC currents and GSC currents. From FIGURE 11 and 12, we can get the main harmonics and total harmonic distortion (THD) rates. Meanwhile, the results were filled into TABLE 1-6. Obviously, the 11^{th} and 19^{th} harmonics in three-phase currents of MSC have increased or maintained under proposed control. But other major harmonics and THD have been reduced. For three-phase currents of GSC, the 2^{th} and 8^{th} harmonics increased obviously. Meanwhile, the 4^{th} harmonic in C-phase current of GSC also slightly increased. However, the decrease of THD and other major harmonics is obvious.

B. SIMULATIONS UNDER VARIABLE WIND SPEED

The variable wind speed is shown in FIGURE 13(a) and the simulation results under proposed control are illustrated in

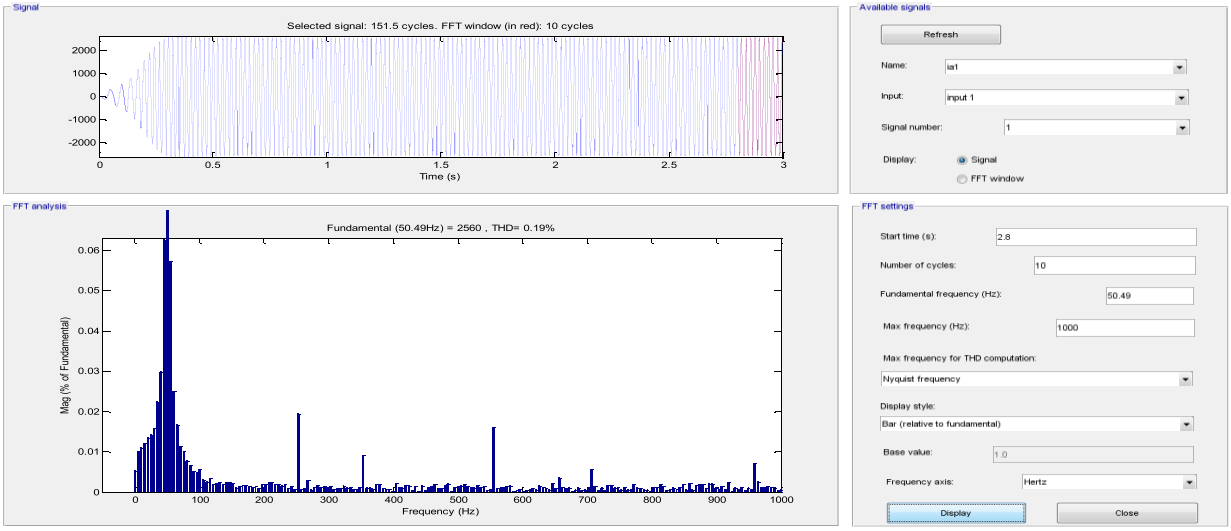

FIGURE 10. FFT analysis GUI.

TABLE 1. A-phase current FFT analysis results of MSC.

Harmonics	4^{th}	5^{th}	7^{th}	8^{th}	10^{th}	$\mathbf{11^{th}}$	13^{th}	14^{th}	17^{th}	$\mathbf{19^{th}}$	THD
Units	‰	‰	‰	‰	‰	‰	‰	‰	‰	‰	%
Conventional control	0.33	0.56	0.37	0.35	0.32	0.09	0.29	0.18	0.1	≤0.05	0.44
Proposed control	≤0.02	0.19	0.08	≤0.02	≤0.02	0.17	≤0.02	0.05	≤0.02	0.05	0.19

TABLE 2. B-phase current FFT analysis results of MSC.

Harmonics	4^{th}	5^{th}	7^{th}	8^{th}	10^{th}	11^{th}	13^{th}	14^{th}	17^{th}	19^{th}	THD
Units	‰	‰	‰	‰	‰	‰	‰	‰	‰	‰	%
Conventional control	0.43	0.43	0.41	0.38	0.40	0.16	0.29	0.18	0.1	0.06	0.49
Proposed control	≤0.02	0.18	0.10	≤0.02	≤0.02	0.16	≤0.02	0.04	≤0.02	0.06	0.19

TABLE 3. C-phase current FFT analysis results of MSC.

Harmonics	4^{th}	5^{th}	7^{th}	8^{th}	10^{th}	$\mathbf{11^{th}}$	13^{th}	14^{th}	17^{th}	19^{th}	THD
Units	‰	‰	‰	‰	‰	‰	‰	‰	‰	‰	%
Conventional control	0.33	0.49	0.37	0.39	0.39	0.12	0.33	0.18	0.09	0.06	0.46
Proposed control	≤0.02	0.20	0.10	≤0.02	≤0.02	0.15	≤0.02	0.05	≤0.02	0.06	0.19

TABLE 4. A-phase current FFT analysis results of GSC.

Harmonics	$\mathbf{2^{th}}$	3^{th}	4^{th}	5^{th}	7^{th}	$\mathbf{8^{th}}$	THD
Units	‰	‰	‰	‰	‰	‰	%
Conventional control	≤0.02	0.03	0.05	0.25	0.19	0.02	0.22
Proposed control	0.07	≤0.02	0.04	0.07	0.04	0.07	0.12

TABLE 5. B-phase current FFT analysis results of GSC.

Harmonics	$\mathbf{2^{th}}$	3^{th}	4^{th}	5^{th}	7^{th}	$\mathbf{8^{th}}$	THD
Units	‰	‰	‰	‰	‰	‰	%
Conventional control	≤0.02	0.03	0.05	0.27	0.19	≤0.02	0.22
Proposed control	0.07	≤0.02	0.04	0.07	0.04	0.07	0.12

FIGURE 13(b)-(h). FIGURE 13(b) shows the wind energy utilization coefficient C_p curve. It is clear that C_P is always maintained at its maximum value C_{P_max} (or 0.476). This means that WECS is in the maximum power point tracking (MPPT) region. FIGURE 13(c) shows the rotor speed curves and FIGURE 13(d) shows the torsion angle θ curve.

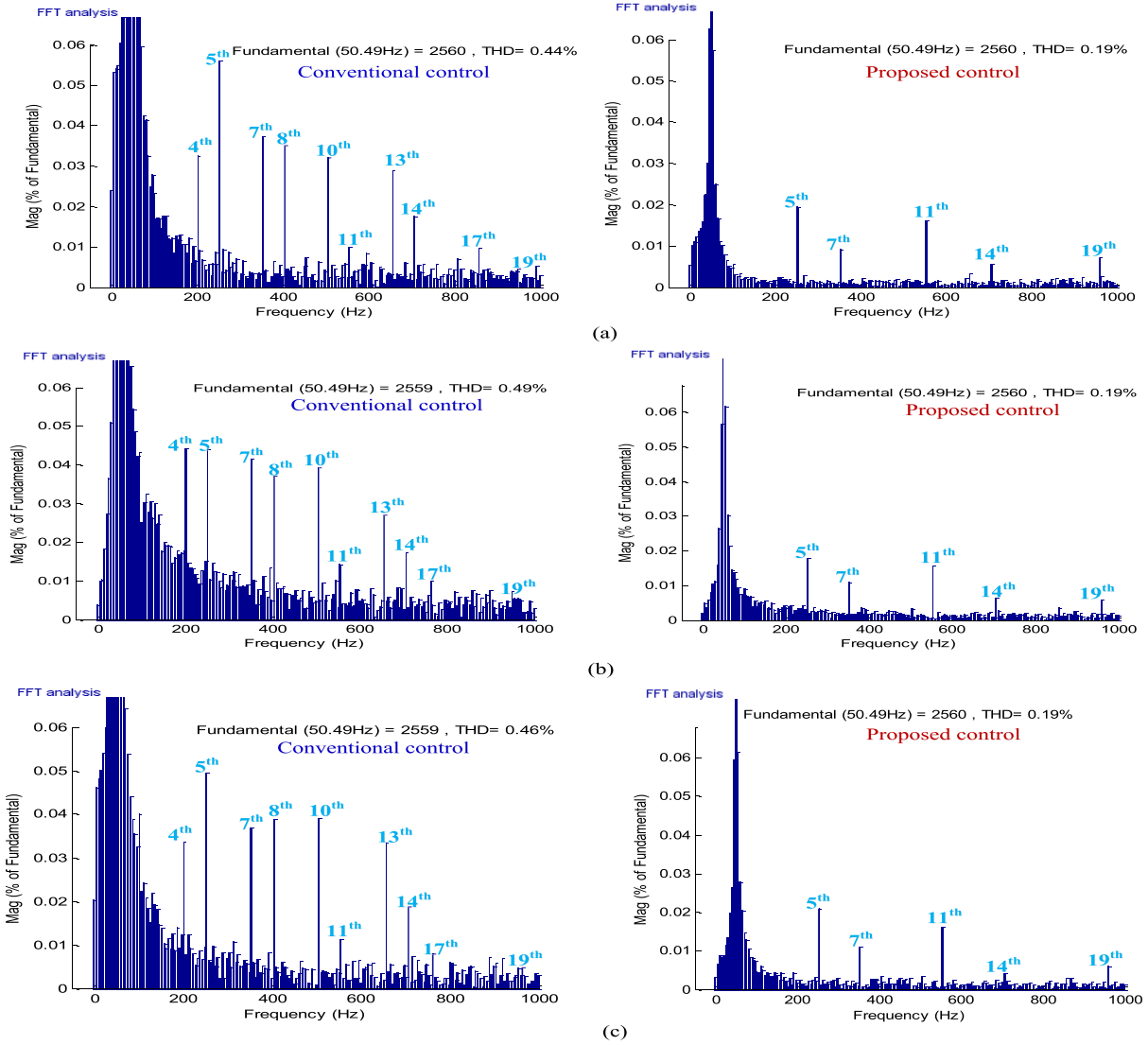

FIGURE 11. FFT analysis of MSC currents.

TABLE 6. C-phase current FFT analysis results of GSC.

Harmonics	**2th**	3th	**4th**	5th	7th	**8th**	THD
Units	‰	‰	‰	‰	‰	‰	%
Conventional control	≤0.02	0.02	≤0.02	0.26	0.18	0.02	0.20
Proposed control	0.07	≤0.02	0.03	0.07	0.04	0.07	0.12

For flexible drive chain, there is a obvious deviation between wind turbine speed ω_{tur} and PMSG speed ω. And the torsion angle θ is defined as

$$\theta = \int_0^t (\omega_{\text{tur}} - \omega)\, dt$$

FIGURE 13(e) shows the DC-link voltage U_{dc} is very close to its reference U_{dc_ref} (or 1800V) and the deviation does not exceed 3V. FIGURE 13(f)-(g) depict the electromagnetic torque curve of PMSG and grid-connected reactive power curve. In general, when the voltage of grid-connected PCC (points of low voltage coupling) is abnormal, the WECS must inject or absorb partial reactive power from the grid. This is the requirement for the construction of a friendly power grid. FIGURE 13(g) indicates that WECS injected 10kvar into power grid during 2s to 4s. The curves of electromagnetic power and grid-connected active power are shown in FIGURE 13(h) and the power curve is shown

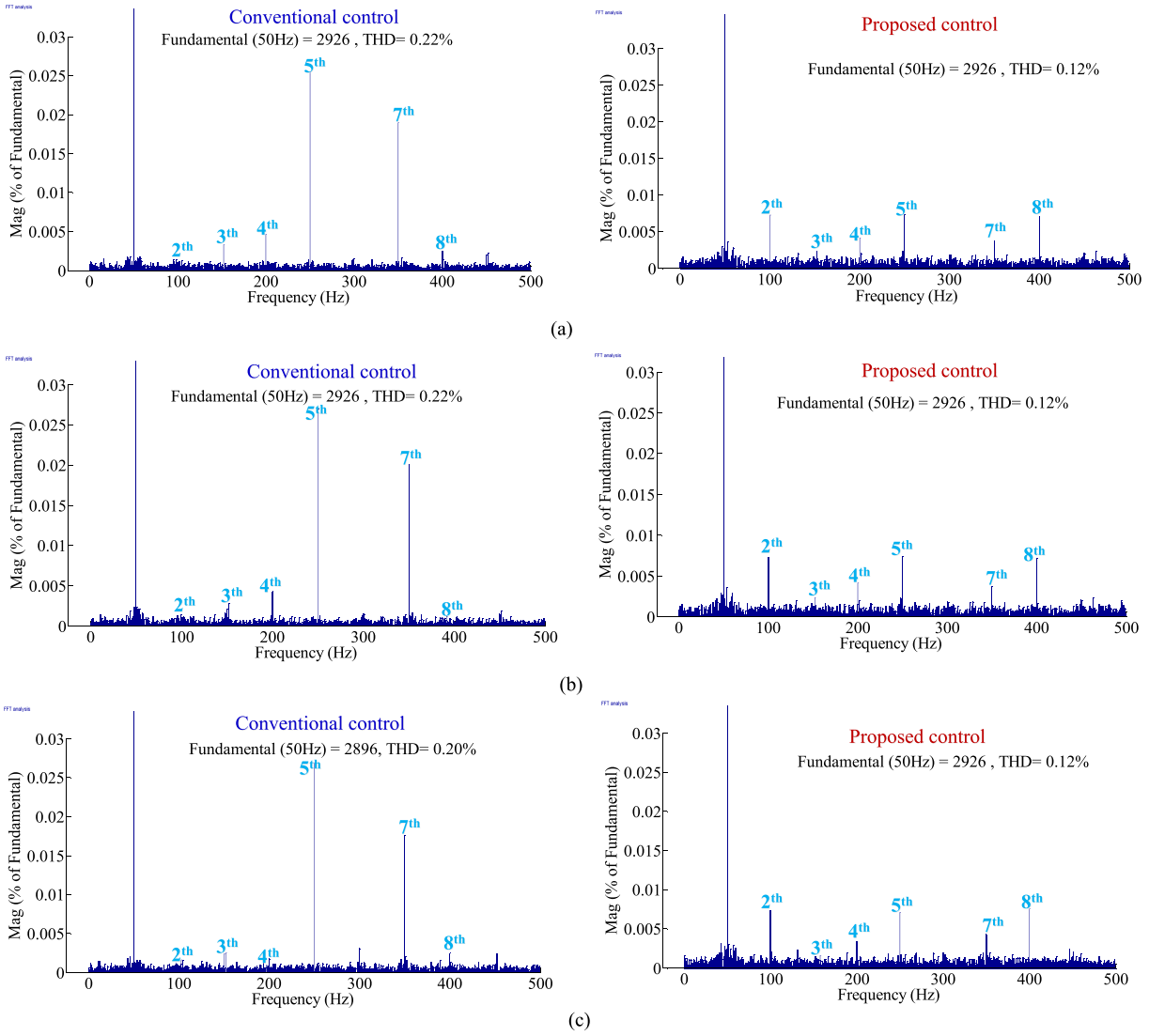

FIGURE 12. FFT analysis of GSC currents.

TABLE 7. Wind Turbine and Flexible Transmission Chain Parameters.

Parameters	Value
Moment inertia of wind turbine J_T [kg·m^2]	2×10^4
Blade length R [m]	31
Air density ρ [kg/m^3]	1.225
Rated wind speed v_{rate} [m/s]	14
Cut-out wind speed v_{Out} [m/s]	25
Maximum utilization coefficient of wind energy $C_{P\ max}$	0.476
Optimal tip speed ratio (OTSR) λ_{opt}	8
Rigidity coefficient of transmission chain K	6.4×10^6
Damping coefficient of transmission chain D	10

TABLE 8. PMSG and Control Parameters.

Parameters	Value
Moment inertia of PMSG J_g [kg·m^2]	700
Rated power P_{rate} [MW]	2
Rated torque T_{rate} [kN·m]	400
Rate rotor speed ω_{rate} [rad/s]	5
Generator pole logarithm	102
Permanent flux [Wb]	1.25
d-axis stator inductor L_d [mH]	8.35
q-axis stator inductor L_q [mH]	8.35
Stator resistance R_s [Ω]	0.01
Central frequency of bandpass filter f_0 [HZ]	120
Damping ratio of bandpass filter ζ	0.707
Injected damping K_D	500
control parameters k	10^6
D_{sd}, D_{sq}, D_{gd} and D_{gd}	500

in FIGURE 13(i). It is clear that the actual power curve fluctuates around the optimal power curve.

V. CONCLUSION

This paper described the application of a robust control strategy to the power control of the PMSG-based WECS. Compared with the conventional control, the robust control strategy has a good robustness for the system uncertainties and can reduce the major harmonics currents, THD of both

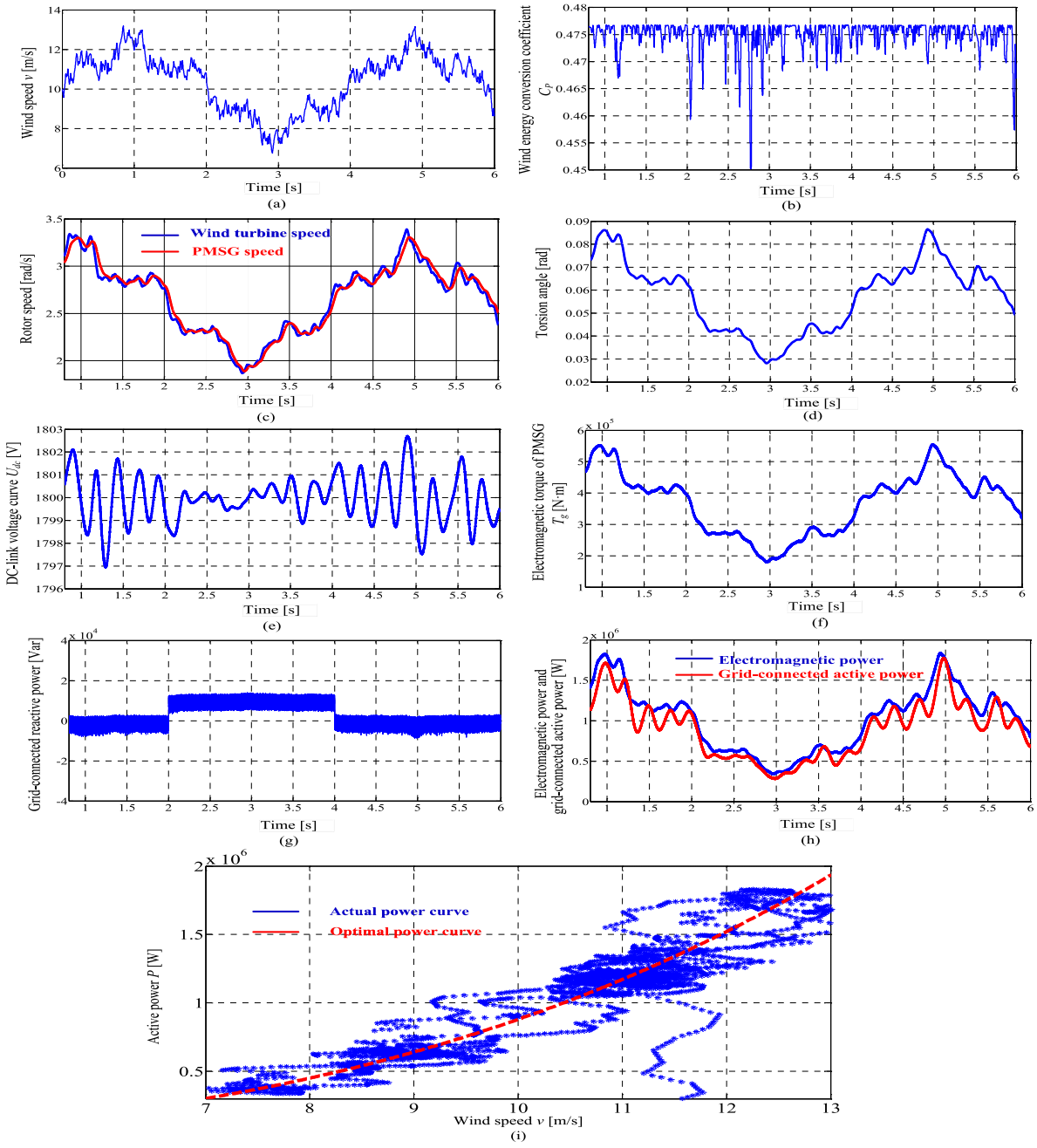

FIGURE 13. System response under variable wind speed.

MSC and GSC currents, and ripples of torque. After that, in order to verify this proposed control algorithm, a 2MW WECS simulation test platform which is relatively close to the actual physical system is built. The effectiveness of the proposed control strategy is verified by a large number of simulation results.

TABLE 9. Dc-link and grid-side system parameters.

Parameters	Value
DC bus voltage U_{dc} [V]	1800
DC bus capacitor C [F]	2.2
System resistance R_c [Ω]	0.001
System inductor L_c [mH]	6
Power grid voltage E_{gd} [V]	380

APPENDIX

See Tables 7–9.

REFERENCES

[1] S. Li, T. A. Haskew, R. P. Swatloski, and W. Gathings, "Optimal and direct-current vector control of direct-driven PMSG wind turbines," *IEEE Trans. Power Electron.*, vol. 27, no. 5, pp. 2325–2337, May 2012.

[2] M. Little and K. Pope, "Performance modelling for wind turbines operating in harsh conditions," *Int. J. Energy Res.* vol. 41, no. 3, pp. 417–428, 2017.

[3] J. Yan, H. Lin, Y. Feng, X. Guo, Y. Huang, and Z. Q. Zhu, "Improved sliding mode model reference adaptive system speed observer for fuzzy control of direct-drive permanent magnet synchronous generator wind power generation system," *IET Renew. Power Gener.* vol. 7, no. 1, pp. 28–35, 2013.

[4] Y. A.-R. I. Mohamed, "Design and implementation of a robust current-control scheme for a PMSM vector drive with a simple adaptive disturbance observer," *IEEE Trans. Ind. Electron.*, vol. 54, no. 4, pp. 1981–1988, Aug. 2007.

[5] R. Errouissi, M. Ouhrouche, W.-H. Chen, and A. M. Trzynadlowski, "Robust nonlinear predictive controller for permanent-magnet synchronous motors with an optimized cost function," *IEEE Trans. Ind. Electron.*, vol. 59, no. 7, pp. 2849–2858, Jul. 2012.

[6] H. Liu and S. Li, "Speed control for PMSM servo system using predictive functional control and extended state observer," *IEEE Trans. Ind. Electron.*, vol. 59, no. 2, pp. 1171–1183, Feb. 2012.

[7] R. Errouissi, A. Al-Durra, and M. Debbouza, "A novel design of PI current controller for PMSG-based wind turbine considering transient performance specifications and control saturation," *IEEE Trans. Ind. Electron.*, vol. 65, no. 11, pp. 8624–8634, Nov. 2018.

[8] L. Shang and J. Hu, "Sliding-mode-based direct power control of grid-connected wind-turbine-driven doubly fed induction generators under unbalanced grid voltage conditions," *IEEE Trans. Energy Convers.*, vol. 27, no. 2, pp. 362–373, Jun. 2012.

[9] S. M. Mozayan, M. Saad, H. Vahedi, H. Fortin-Blanchette, and M. Soltani, "Sliding mode control of PMSG wind turbine based on enhanced exponential reaching law," *IEEE Trans. Ind. Electron.*, vol. 63, no. 10, pp. 6148–6159, Oct. 2016.

[10] C. Evangelista, P. Puleston, F. Valenciaga, and L. M. Fridman, "Lyapunov-designed super-twisting sliding mode control for wind energy conversion optimization," *IEEE Trans. Ind. Electron.*, vol. 60, no. 2, pp. 538–545, Feb. 2013.

[11] J. Yang, S. Li, and X. Yu, "Sliding-mode control for systems with mismatched uncertainties via a disturbance observer," *IEEE Trans. Ind. Electron.*, vol. 60, no. 1, pp. 160–169, Jan. 2013.

[12] R. Errouissi and A. Al-Durra, "A novel PI-type sliding surface for PMSG-based wind turbine with improved transient performance," *IEEE Trans. Energy Convers.*, vol. 33, no. 2, pp. 834–844, Jun. 2018.

[13] E. A. Bossanyi, "The design of closed loop controllers for wind turbines," *Wind Energy*, vol. 3, no. 3, pp. 149–163, Sep. 2000.

[14] E. A. Bossanyi, "Wind turbine control for load reduction," *Wind Energy*, vol. 6, no. 3, pp. 229–244, 2003.

[15] E. A. Bossanyi, "Controller for 5MW reference turbine," UpWind, Falmouth, U.K., Tech. Rep. 11539/BR/04, Jul. 2009.

[16] F. Zhang, W. E. Leithead, and O. Anaya-Lara, "A combined controller design of power system stabilizer and wind turbine drive-train damping filter," in *Proc. Int. Conf. Sustain. Power Gener. Supply*, Sep. 2012, pp. 1–6.

[17] J. Licari, C. E. Ugalde-Loo, J. B. Ekanayake, and N. Jenkins, "Damping of torsional vibrations in a variable-speed wind turbine," *IEEE Trans. Energy Convers.*, vol. 28, no. 1, pp. 172–180, Mar. 2013.

[18] A. D. Hansen and G. Michalke, "Modelling and control of variable-speed multi-pole permanent magnet synchronous generator wind turbine," *Wind Energy*, vol. 11, no. 5, pp. 537–554, 2008.

[19] T. Orlowska-Kowalska and K. Szabat, "Damping of torsional vibrations in two-mass system using adaptive sliding neuro-fuzzy approach," *IEEE Trans. Ind. Inform.*, vol. 4, no. 1, pp. 47–57, Feb. 2008.

[20] R. Muszynski and J. Deskur, "Damping of torsional vibrations in high-dynamic industrial drives," *IEEE Trans. Ind. Electron.*, vol. 57, no. 2, pp. 544–552, Feb. 2010.

[21] A. Lorenzo-Bonache, A. Honrubia-Escribano, and F. Jiménez-Buendía, "Generic type 3 wind turbine model based on IEC 61400-27-1: Parameter analysis and transient response under voltage dips," *Energies*, vol. 10, no. 9, p. 1441, 2017.

[22] L. Trilla, F. D. Bianchi, and O. Gomis-Bellmunt, "Linear parameter-varying control of permanent magnet synchronous generators for wind power systems," *IET Power Electron.*, vol. 7, no. 3, pp. 692–704, 2014.

[23] K.-H. Kim, Y.-C. Jeung, D.-C. Lee, and H.-G. Kim, "LVRT scheme of PMSG wind power systems based on feedback linearization," *IEEE Trans. Power Electron.*, vol. 27, no. 5, pp. 2376–2384, May 2012.

[24] I. P. Girsang, J. S. Dhupia, E. Muljadi, M. Singh, and J. Jonkman, "Modeling and control to mitigate resonant load in variable-speed wind turbine drivetrain," *IEEE J. Emerg. Sel. Topics Power Electron.*, vol. 1, no. 4, pp. 277–286, Dec. 2013.

[25] J. Liu, H. Meng, Y. Hu, Z. Lin, and W. Wang, "A novel MPPT method for enhancing energy conversion efficiency taking power smoothing into account," *Energy Convers. Manage.*, vol. 101, pp. 738–748, Sep. 2015.

FEIHANG ZHOU was born in Xi'an, China, in 1989. He received the bachelor's degree from Xi'an Polytechnic University and the master's degrees from the Xi'an University of Technology, where he is currently pursuing the Ph.D. degree.

His current research is performance optimization control and torsional vibration analysis and suppression for large permanent magnet synchronous wind turbine units.

JUN LIU was born in Xi'an, China, in 1963. He graduated from Xi'an Jiaotong University and Xi'an University of Technology. He is currently a Professor with the Xi'an University of Technology.

He has a long-term research and teaching on wind power, power drag technique, and intelligent control. And, he has accumulated some valuable experience from his research.